PROVIDING STRINGENT STAR FORMATION RATE LIMITS OF z~2 QSO HOST GALAXIES AT HIGH ANGULAR RESOLUTION

Andrey Vayner[1,2], Shelley A. Wright[1,2], Tuan Do[2,6], James E. Larkin[3], Lee Armus[4], Sarah C. Gallagher[5]

Draft version October 23, 2014

ABSTRACT

We present integral field spectrograph (IFS) with laser guide star adaptive optics (LGS-AO) observations of z=2 quasi-stellar objects (QSOs) designed to resolve extended nebular line emission from the host galaxy. Our data was obtained with W. M. Keck and Gemini-North Observatories using OSIRIS and NIFS coupled with the LGS-AO systems, respectively. We have conducted a pilot survey of five QSOs, three observed with NIFS+AO and two observed with OSIRIS+AO at an average redshift of z=2.15. We demonstrate that the combination of AO and IFSs provides the necessary spatial and spectral resolutions required to separate QSO emission from its host. We present our technique for generating a PSF from the broad-line region of the QSO and performing PSF subtraction of the QSO emission to detect the host galaxy emission at separation of $\sim 0.2''$ ($\sim$1.4 kpc). We detect Hα and [NII] for two sources, SDSS J1029+6510 ($z_{H\alpha}$=2.182) and SDSS J0925+06 ($z_{H\alpha}$=2.197), that have both star formation and extended narrow-line emission. Assuming that the majority of narrow-line Hα emission is from star formation, we infer a star formation rate for SDSS J1029+6510 of 78.4 $M_\odot$ yr^{-1} originating from a compact region that is kinematically offset by 290 - 350 km s^{-1}. For SDSS J0925+06 we infer a star formation rate of 29 $M_\odot$ yr^{-1} distributed over three clumps that are spatially offset by $\sim$ 7 kpc. The null detections on three of the QSOs are used to infer surface brightness limits and we find that at 1.4 kpc distance from the QSO that the un-reddened star formation limit is $\lesssim 0.3$ $M_\odot$ yr^{-1} kpc^{-2}. If we assume a typical extinction values for z=2 type-1 QSOs, the dereddened star formation rate for our null detections would be $\lesssim 0.6$ $M_\odot$ yr^{-1} kpc^{-2}. These IFS observations indicate that while the central black hole is accreting mass at 10-40% the Eddington rate, if star formation is present in the host (1.4 - 20 kpc) it would have to occur diffusely with significant extinction and not in compact, clumpy regions.

Subject headings: quasars: feedback - galaxies: high-redshift - galaxies: kinematics and dynamics

1. INTRODUCTION

Understanding the formation and growth of supermassive black holes (SMBH) with galaxy evolution is a key problem in astrophysics. Some of the largest puzzles are the origin of M-σ relationship (Magorrian et al. 1998, Gebhardt et al. 2000), the role of active galactic nuclei (AGN) feedback and its effects for quenching star formation (e.g., Scannapieco et al. 2005; Barai et al. 2014), and how to effectively transport gas to the galactic nuclei to fuel black hole growth (e.g., Thompson et al. 2005; Hopkins & Quataert 2011).

The majority of quasi-stellar object (QSO) host galaxy studies have concentrated on nearby systems (z$\lesssim$0.4) using optical observations with Hubble Space Telescope (HST) and ground-based facilities (e.g., Bahcall et al. 1997; Lehnert et al. 1999; Hamilton et al. 2002; Hutchings et al. 2002; Ridgway et al. 2002; Márquez & Petitjean 2003; Zakamska et al. 2006; Floyd et al. 2010, 2013). The key ingredient in these observations are to achieve the high spatial resolutions necessary to disentangle bright QSO emission to that of the underlying stellar population and star formation. A range of host galaxy parameters have been discovered with QSOs that reside in massive inactive elliptical galaxies to that of QSOs that reside in late-type spirals and irregulars, and galaxies with a range of simultaneous star formation activity (e.g, Bennert et al. 2008). Even with the large range of selection effects, there is a coherent picture that luminous nearby QSOs are generally found in luminous and massive host galaxies with a range of morphologies (Matsuoka et al. 2014). However, at high-redshift (z$\gtrsim$1) the picture of QSO host galaxies is less clear with only a small number of host systems observed. High redshift QSOs have been found in star forming galaxies with morphologies ranging from discs (e.g., Inskip et al. 2011) to mergers (e.g. Carniani et al. 2013; Floyd et al. 2013), while some studies have shown to reside in passive, elliptical galaxies (e.g. Kotilainen et al. 2009).

One of the most compelling physical explanations of the co-evolution of the host galaxy and SMBH is negative feedback from AGN energetics. There has been mounting observational evidence supporting star formation quenching via QSO/AGN activity by expelling large reservoirs of cold gas and/or heating of the gas in massive halos (Fabian 2012, references therein). Recent studies have found that the majority of their low redshift type-2 QSOs (z$\sim$ 0.2) contain evidence of galaxy wide outflows

[1] Department of Astronomy & Astrophysics, University of Toronto, 50 St. George street, Toronto, ON, M5S 3H4
[2] Dunlap Institute for Astronomy & Astrophysics, University of Toronto, 50 St. George street, Toronto, ON, M5S 3H4
[3] Department of Physics and Astronomy, University of California, Los Angeles, CA 90095
[4] Spitzer Science Center, California Institute of Technology, 1200 E. California Blvd., Pasadena, CA 91125
[5] Department of Physics and Astronomy, The University of Western Ontario, London, ON N6A 3K7
[6] Dunlap Fellow

on kpc scales with [OIII] emission lines (Harrison et al. 2014; Liu et al. 2013), however their effects on the star formation rates are yet to be understood. Similarly, recent integral field spectrograph (IFS) observations of [OIII] & Hα emission in z$\sim$2 QSOs have revealed host galaxies with strong evidence of outflows that have indicated lower star formation rates in regions with strongest outflows (Gemini NIFS: Alexander et al. 2010, VLT SINFONI: Cano-Díaz et al. 2012). These observations have given tantalizing clues of QSO feedback, yet there is still little known about the z$\sim$2 host galaxies (i.e, stellar mass, dynamics, metallicities), and whether they obey the present day black hole mass-galaxy scaling relations (McConnell & Ma 2013).

QSOs outshine their host galaxy by several orders of magnitude and to study their hosts require careful removal for which a good understanding of the point spread function (PSF) is required. Understanding the PSF for ground based observations is very difficult, atmospheric variations cause the PSF to change over a time span of a few seconds making it extremely difficult to model. Using nearby stars as reference there has been some successful attempts to remove the bright QSO light and extended emission from the host galaxy was detected (e.g., seeing-limited:Falomo et al. 2004; Kotilainen et al. 2009; Schramm et al. 2008 AO: Falomo et al. 2005). The majority of QSO host galaxy observations have used space-based observations where the PSFs are stable for QSO removal. At low redshift (z$\lesssim$1) there have been several studies that used both artificial and stellar PSF to remove QSO light to search for extended emission, which have allowed for several successful studies of low & intermediate redshift QSO hosts (Bahcall et al. 1997, Kirhakos et al. 1999, Hutchings et al. 2002). At high-redshift (1 $\lesssim$ z $\lesssim$4), these searches have been more challenging since the angular scales of host galaxies are comparable to the PSF halo ($\sim$1$''$) and PSF removal is dominated by residuals, which makes it difficult to disentangle the QSO and host galaxy. The bigger difficulty comes from extracting star formation rates(SFR) and metalicities of the host galaxies, since these quantities can be easily contaminated from QSO narrow-line emission with a range of spatial and kinematic offsets ($\lesssim$ 1000 km s^{-1};Cano-Díaz et al. 2012, Liu et al. 2013). Broad-band photometry has been used to model the stellar properties of the distant host galaxies, however residual noise from PSF subtraction makes it difficult to obtain accurate magnitudes, and there are no reliable tests to distinguish stellar rest-frame optical continuum from synchrotron from the central AGN.

A combination of adaptive optics (AO) and integral field spectroscopy (IFS) provides the necessary spatial and spectral resolutions required to separate QSO emission from its host. Having spectral information at each spatial location allows us to extract key information about the galaxy that an imaging survey simply cannot achieve. IFS observations provide a powerful technique to remove the bright QSO. This can be achieved by utilising unresolved emission from the QSO (i.e., broad-line emission, like Hα) to construct a pure QSO PSF image. This PSF image is normalized and then subtracted per wavelength channel in the data cube, thus leaving only narrow-line emission. If there is spatially offset narrow-

line emission, this can be used directly to infer kinematics, dynamical masses, and nebular emission diagnostics of the gas. Recently this technique was proven to be effective in resolving a host galaxy of a redshift (z=1.3) QSO using SINFONI on the VLT (Inskip et al. 2011). These authors were successful at detecting the host galaxy and were able to construct a spatially resolved narrow emission line map with identified ionization mechanisms and star formation rates(100 M$_\odot$ yr^{-1}). They found that the galaxy dynamical mass and black hole mass obeyed the present-day M$_{BH}$ vs. M$_{bulge,stellar}$ relation within the current scatter. In contrast, there have been no IFS observations of high-z QSOs hosts where the central AGN has been shown to regulate star formation. While evidence for QSO driven winds at low and high-redshifts have been found, only a single case has shown direct evidence that suggests these winds regulate the star formation (Cano-Díaz et al. 2012). Clearly, the necessity of a larger sample of high-z QSO host galaxy observations are needed to build-up a coherent picture.

We have conducted an IFS LGS-AO pilot survey of five z$\sim$2 type-I QSOs using both Keck II and Gemini North facilities to demonstrate the feasibility and limits of QSO host galaxy detection at high-redshift and to have a range of QSO properties. In §2 we describe the observations and target selection. In §4 we describe our PSF extraction and removal technique, in §5 we discuss about our two sources which had a narrow Hα detection and describe how we obtained our flux limits in sources with null detections, in §6 we interpret the results on two of our sources SDSS1029+6510 & SDSS0925+06 and derive dust corrected star formation limits. Finally we put our results in context of studies that look at systems with similar bolometric luminosities and in §7 we provide our conclusions. Throughout the paper we assume Λ-dominated cosmology with Ω_M=0.31, Ω_Λ=0.70, and H$_o$=67.8 km s^{-1} Mpc^{-1} (Planck Collaboration et al. 2013).

2. OBSERVATIONS

We used the near infrared integral field spectrographs OSIRIS (Larkin et al. 2006) on the Keck telescope and NIFS (McGregor et al. 2003) on the Gemini north telescope (GN-2012B-Q-53) coupled with the observatories' laser guide star adaptive optics systems. We present K-Band spectra of 5 quasars at an average redshift of z $\approx$ 2.2 (8.42 kpc per arcsecond) with data taken on December 30 2011 - January 1st 2012 at the Keck observatory and on August 2012 − January 2013 at Gemini North with an average total on target integration time of 3400s. Table 1 summarizes our observational parameters and setup.

2.1. *Target Selection*

We selected these QSO from the fifth edition of the SDSS quasar catalog based on the seventh data release (Schneider et al. 2010). For this pilot survey we selected sources that would have optimal AO performance to aid in the PSF subtraction. The best QSOs to target were selected based on the following criteria for the Keck and Gemini North observations: (1) all objects must be observable with the Altair and Keck AO system based on tip/tilt magnitude and separations, and (2) objects must have redshift between 2.016 and 2.427 where Hα falls in

the prime K-band wavelength regime ($< 2.2\ \mu$m). Using these constraints at K-band allowed only ~30 observable QSOs. We targeted the best of these sources, one with on-axis tip-tilt source correction (R=16.4 mag), and four with ideally located bright stars for off-axis tip-tilt correction. Table 1 contains all the information on the tip/tilt stars. All of our selected sources are Type 1 radio quiet QSOs with 1.4 GHz flux < 0.15 mJy (Becker et al. 1995), with no prior spectral knowledge in the IR, making our sample less biased towards QSO hosts with high star formation rates. Table 2 contains archival photometric information. Using the SDSS spectra (Figure 1), we derive the average redshift (z_{UV}), bolometric luminosity (L_{Bol}), black hole mass (M_{BH}), and Eddington ratio for each QSO, and this is presented in Table 3.

In Table 4 we present redshifts of the UV emission lines derived in fifth quasar catalog based on the 7th data release (Schneider et al. 2010). In certain cases we find that the redshift of the broad Hα is offset by $1,500 \mathrm{km\,s^{-1}}$ from the UV derived redshift. We find that the more luminous QSOs in our sample have a stronger offsets. Using our K band QSO spectra we derive the luminosity of the broad Hα emission line, black hole mass and the equivalent width (Table 5).

3. DATA REDUCTION
3.1. *OSIRIS*

The OSIRIS observations were reduced using the OSIRIS reduction pipeline. Dark frames were median combined to produce a master dark frame using the OSIRIS pipeline. Each frame then had the master dark subtracted from it and the following basic routines were run: adjust channel level, remove crosstalk, clean cosmic rays, and correct for dispersion, the pipeline then reformatted the 2D spectra into a 3D data cubes. The science frames had the nearest sky frame in time subtracted from them using the scaled sky subtraction routine to adjust the intensity of the OH lines to account for the temporal variability of the sky lines (Davies 2007). The science and telluric frames were stacked together using a 3σ mean clip algorithm inside the mosaic frames routine. A 1D telluric spectrum was then extracted from the highest signal to noise spaxels in the telluric cube using the extract star routine. Strong hydrogen absorption lines were masked, and the blackbody of the star was subtracted out using the remove hydrogen lines and divide blackbody routines. The spectra were then normalized and used to correct for atmospheric absorption in the mosaiced science frame. The final science data cube was flux calibrated using standard star observations closest in time and air mass which were reduced in the same manner as above.

3.2. *NIFS*

The NIFS observations were reduced using the Gemini NIFS IRAF reduction pipeline that operates within Pyraf [7]. Some modifications were applied to the standard pipeline and additional routines were written to match our science goals. For each night we reduced the Xe, Ar lamp observations to establish the wavelength solution for each of the targets using the Gemini NIFS Pyraf

[7] http://www.gemini.edu/sciops/instruments/nifs/data-format-and-reduction

baseline calibration routine. Dark frames for the science observations were median combined and subtracted from each of the science and sky frames. The science, telluric, and sky frames were then reduced using the NIFS science reduction routine. The end result is a data cube which has been flat fielded, bad pixel masked and reformatted into a 3D cube which was spatially re-sampled to square pixels with a size of $0.05''$ from the native spatial sampling of of $0.1 \times 0.04''$. The science and telluric frames had the nearest sky frame in time subtracted, with OH emission line scaling between the sky and science frames. The centroids of the QSO and telluric stars were obtained through a 2D Gaussian fit to a spectrally collapsed image, and the dithered observations were shifted and stacked using an 3σ mean clipped algorithm. The 1D telluric star spectrum was extracted by averaging spatially over the highest signal-to-noise spaxels, its blackbody was subtracted, and the strong hydrogen absorption line were masked. The 1D telluric spectrum was then divided into the science cube to correct for atmospheric and instrumental absorption features.

4. EXTRACTING THE QSO HOST GALAXY

All five QSOs have broad-line Hα emission that is used for PSF subtraction to remove the QSO emission and continuum from the data cube. We measure broad-line Hα equivalent width and redshift and dereive the Hα luminosity and subsequent black hole masses, ranging from $10^{9-11}\ \mathrm{M_\odot}$. These H$\alpha$ broad-line properties are listed for each QSO in Table 5.

The broad Hα emission originates from gas located in compact accretion disks making this emission essentially point-like in our observations. We use the spectral channels that confine the broad line emission for PSF construction. Our algorithm checks for the highest signal-to-noise spectral channels that do not coincide with OH emission lines to be combined to create a master PSF image. Generally the selected PSF regions are 2.5-3 nm (10 - 15 spectral channels) in size and tend to sit near the peak of the broad Hα line. The combination occurs with a three sigma mean clipping routine to remove any potential inclusion of narrow line emission flux. The end result is a 2D image of our observed PSF that gets normalized to the flux by the max pixel. We then go through individual channels in our data cube, scale the image to the maximum value of the PSF at the particular channel and subtract the image. This routine provided the best residuals post PSF subtraction cubes. Some studies have additional steps with PSF construction, by additionally fitting and subtracting the nuclear continuum with a low order polynomial (Inskip et al. 2011). The purpose of the linear fit is to remove any continuum emission from the host galaxy. In our work, extensive studies of the final PSF subtracted cube using both methods does not reveal a continuum emission from the host galaxy at the 3σ level (average K mag > 20.9), hence we decided not to include this additional step in our QSO PSF construction routine since it adds at least 1.2 times more noise in the PSF subtracted cubes. To test the quality of our PSF subtraction, we constructed radial profiles at different wavelength channels, before and after PSF subtraction, to verify whether the final cube had the central core and seeing halo successfully removed. Figure 2 shows the results of these tests for two

of our targets, the green and blue radial profile curves are constructed from a spectrally-collapsed image which contain both broad and narrow Hα emission, while the red curve is constructed from just the PSF image. These figures demonstrate that the PSF subtracted data has a significant portion of the QSO flux removed, with only the inner $0.2''$ being strongly dominated by noise from PSF subtraction. Averaging over the data cube along the spectral axis, we find that generally within $0.2''$ the QSO still contributes to about 10-20% of the total data counts, while outside $0.2''$ only 2-5%. As expected the observations with the best PSF FWHM showed the best post PSF subtraction data cubes. However it should be noted that left over QSO continuum/BLR light does not affect measured values derived from narrow line emission, since they are derived by fitting the line and any under-line continuum left over from PSF subtraction simultaneously, at which stage the continuum contamination can be calculated.

5. RESULTS

To find narrow line emission we have systematically search all of the individual $\sim 3{,}000$ spaxels in each of the cubes. When a line feature is identified we calculated the signal-to-noise by obtaining the standard deviation in the surrounding spatial and spectral pixels, and divided it into the fitted peak of the emission line. For cases where a faint emission feature is found we bin the data using nearby spaxels to increase the signal-to-noise to distinguish between a faint noise spike versus real emission. For bright noise spikes we wrote a routine that parses through the cube and removes them if their counts are 5σ or higher from the standard deviation in the surrounding region (both spatially and spectrally). This routine also confirms faint extended structure in the case of SDSS0925+06 to be real rather than a combination of separated noise spikes. After searching through the five observed data cubes we identify narrow line emission in two of the systems. We confirm a detection if the peak of the emission line is greater than 3σ and the spectral width is greater than the intrinsic instrumental width. For the given QSO redshift, the identified emission lines are likely narrow Hα since it is the brightest narrow emission line in our spectral range. Once a line is identified we searched for [NII] & [SII] at a similar velocity offset from the broad Hα line. The detected narrow Hα emission lines all lie within $600~\mathrm{km\,s^{-1}}$ from their respective QSOs, however the full spectral axis in each spaxel was examined for a potential narrow emission lines that could be associated with structure surrounding our QSOs.

5.1. *OSIRIS: SDSS 1029+6510*

Figure 3 (panel I) shows the K-Band image of the SDSS 1029+6510 QSO from the collapsed data cube (1.99-2.4 μm). Figure 3 (panel II) and Figure 3 (panel III) shows the 2D kinematics of the extended narrow line emission relative to the broad Hα emission and the spectrum of the individual components, respectively. The PSF subtracted data cube reveals three extended narrow line emission regions, we label them A,B & C in Figure 3 (panel II). These emission-line regions have a blue-shifted velocity offset of 10-500 $\mathrm{km\,s^{-1}}$ with respect to broad Hα emission, and have a maximum projected

separation of $\sim 0.6''$(4.2 kpc) from the QSO. We bin the individual spaxels in regions A & C to detect Hα emission at a signal-to-noise of 3.1 and 2.1, respectively. Individual spaxels in region B reach a signal-to-noise of $\gtrsim 2$, with the central 3 pixels reaching a signal to noise $\gtrsim 7$. In Table 6 we present the extracted emission-line properties of the individual regions. Based on the ratio of log([NII]/Hα) for A, this region can reside in the transition zone between AGN/SF in the HII diagnostic (or BPT) diagram (Figure 6). Assuming no extinction, the star formation rate limit for Hα flux in region A is $11.0\pm2.3~\mathrm{M_\odot~yr^{-1}}$ using the Schmidt-Kennicutt law $(\mathrm{SFR}_{H\alpha} = \frac{L_{H\alpha}}{1.26\times10^{41}}$ Kennicutt 1998). Region B is located well in the star formation position on the BPT (log([NII]/Hα)<-1.5) diagram with a star formation rate of $67.4\pm5.7\mathrm{M_\odot~yr^{-1}}$. Region C resides well inside the AGN component of the BPT diagram, and therefore is likely narrow line emission from the QSO, at a radial distance of $\sim$2.8 kpc.

5.2. *NIFS: SDSS 0925+06*

Figure 4 (panel I) is a K-Band image of the QSO constructed by summing the flux across the entire data cube (1.99-2.4 μm). Figure 4 (panel II and III), show the 2D kinematics of the extended narrow line emission relative to the redshift of the broad Hα emission and the spectra of the individual components, respectively. The post PSF subtracted data cube reveals resolved narrow Hα emission originating from three distinct regions (A, B, and C), that are both spatially offset ($0.5''$-$1''$) and redshifted (80-250 $\mathrm{km\,s^{-1}}$) from the QSO, see Table 7 for extracted parameters on individual regions . We bin by $0.25''\times0.25''$for each of these regions to build-up the signal-to-noise for kinematic analysis. Limits on the log([NII]/Hα) ratio places region A inside the SF region on the BPT diagram while regions B&C can still be partially ionized by the QSO (see Figure 6). Our limits allow us to discard shocks contribution to the emission for regions A,B,&C (Allen et al. 2008). Using the Schmidt-Kennicutt law (Kennicutt 1998) we obtain an un-reddened upper limit star formation rates of 13±2.3, 12.0±0.5, 4.0±0.4 $\mathrm{M_\odot~yr^{-1}}$ for regions A,B & C, respectively. Assuming these three clumps have virialized we obtain dynamical masses of 8.7,1.0,0.3 $\times10^9\mathrm{M_\odot}$ (Table-7)

5.3. *Null detections: SDSS1005+4346, SDSS2123-00 & SDSS0850+58*

The remaining three targets reveal no narrow-line Hα emission offset spatially or spectrally from the QSO. Null detections may be due to two possibilities: (1) these sources have heavy extinction azimuthally around the QSO $\gtrsim$1 kpc; and/or (2) these sources have sufficiently low star-formation rates that reside below the sensitivity limit of these observations.

We perform a Monte-Carlo simulation in which we generate star forming regions with narrow-line Hα emission surrounding the QSO at various spatial separations. The purpose of these simulations are to find the limiting flux (and unreddened star-formation rate) of our observations and determine how well our PSF removal techniques effect our sensitivity versus the distance from these QSOs. For our simulations, individual star-forming

regions occupy $0.2'' \times 0.2''$ in the OSIRIS data cube and $0.25'' \times 0.25''$ in the NIFS data cube, with each spaxel containing a spectrum consisting of an emission line resembling narrow Hα with a full width at half max of 80 km s^{-1}. The total flux vary in the star forming regions in each data cube, however in individual data cubes all star forming regions have the same flux. We insert these regions uniformly surrounding the QSO in a cross shape to resemble resolved extended structure, which ranged from $0.1''$ to $1.5''$ in separation from the QSO in the NIFS data cubes and $0.1''$-$0.7''$ in the OSIRIS cubes. The spacing between the star forming regions is $0.1''$ to allow signal-to-noise estimates surrounding each individual region. We vary the star formation rates from 0.5 M$_\odot$ yr^{-1} to 40 M$_\odot$ yr^{-1} in each of the narrow-line emission regions. We then process the data cubes through the reduction pipeline as described in §3. Finally we run our PSF subtraction routine on the reduced data cubes the same way as described in §4. We attempt to recover each of the narrow-line Hα emission that were artificially inserted, the detection criteria is the same as for the real data, the emission must be detected with a minimum of a 3σ confidence and the emission lines must have a FWMH greater than the instrumental width.

The recovered star-forming regions with the minimum star-formation rates at various angular separations are presented in Figures 7 and 8, the fluxes of Hα from regions A,B, and C are also over plotted from SDSSJ0925+06 and SDSSJ1029+6510 for comparison. In general we find that our data reduction procedure is not the main factor for low narrow Hα flux, the dominant effect is the sensitivity of the detector and PSF removal within $0.2''$ from the QSO. At separations $> 0.2''$ the limiting star-formation rates is at an average of 1.4 M$_\odot$ yr^{-1} (0.7×10^{-17}erg s^{-1} cm^{-2}) integrated over a star-forming region for the NIFS instrument and 1.5M$_\odot$ yr^{-1} for OSIRIS, this translates to 0.32M$_\odot$ yr^{-1} kpc^{-2} and 0.53M$_\odot$ yr^{-1} kpc^{-2} in the NIFS and OSIRIS data cubes respectively.

For SDSSJ0925+06 the flux of the observed components sit well above the star formation distribution (Figure 7), and in principle we are able to detect emission fainter at smaller separations. For SDSSJ1029+6510, we show the integrated flux of region B as well as its individual components in Figure 8, and find they are detected without binning. Based on these simulations and the limiting flux that both of these sources have, indicates low Hα flux at near and far angular separations from the QSOs. In addition, the other three QSOs do not show any signs of Hα narrow-line emission.

The bolometric luminosities of our sample all sit near 1×10^{47}erg s^{-1} cm^{-2}, the maximum value for a z$\sim$2 QSO is around 1×10^{48}erg s^{-1} cm^{-2} as have been found by studies such as Croom et al. 2009. This limit allows us to only correct for 2.5 magnitudes of extinction at 1450Å, allowing the limiting star formation rates to get as large as 2.03 M$_\odot$ yr^{-1}(0.5M$_\odot$ yr^{-1} kpc^{-2}) or 2.2 M$_\odot$ yr^{-1}(0.8M$_\odot$ yr^{-1} kpc^{-2}) for NIFS and OSIRIS respectively (see §6.1, 6.2). Note that only for the case of SDSS0925+06 the limits may be higher as the QSO is intrinsically redder than the rest of our sample (see §6.2). We acknowledge that the dust in these scenarios is uniformly distributed hence the same dust proprieties that

we find along the line of site of the QSO are else where in the galaxy. Most studies that quote star formation rates give them integrated over some angular scale, typically the beam size of their instrument if the sources they are referencing are not resolved. At the angular resolution of our observations we are capable of resolving a typical z$\sim$2 galaxy which tend to have an angular scale of $\sim 1''$. Integrating these limits over a $1''$ box we obtain for NIFS: 22.57M$_\odot$ yr^{-1}(32.72M$_\odot$ yr^{-1} with maximum dust extinction), OSIRIS: 37.39 (54M$_\odot$ yr^{-1} with maximum dust extinction). We think that these are hard limits on the upper value of the star formation rate in these host galaxies. The derived SFR limits include contamination from dust in the AGN, there is a possibly that most of the dust is surrounding the nuclear region rather than in the host galaxy, as we find that mid-IR WISE magnitudes are significant, indicating that a a large portion of the dust maybe AGN heated. Limits closer to the value with minimum dust (22.57M$_\odot$ yr^{-1} for NIFS and 37.39M$_\odot$ yr^{-1} for OSIRIS) may be more realistic, as some previous studies of dust in type-1 luminous QSOs near z$\sim$2 have found a number of sources with very little (A$_V$ <0.01) to no extinction.

6. DISCUSSION

There are two explanations for the null Hα narrow-line emission detections in our sample. This could be caused simply by the lack of star formation and/or significant extinction in the host galaxy. We argue that the main reason for why we do not see a significant amount of narrow Hα is likely due to the lack of star formation rather than extinction since multi-wavelength observations indicates that our sources do not contain sufficient amount of dust to cause the observed Hα limits. The QSOs in our sample are all luminous type-1 AGNs representing some of the most powerful QSOs at z$\sim$ 2. As we will argue in the following sections even a small dust correction to these systems will increase the bolometric luminosities of our objects above the observed values at this redshift. This indicates that the majority of QSOs in our sample are hosted inside galaxies that are either in a phase of transitioning to-or-from star forming activity or reside in quiescent galaxies.

6.1. *SDSS 1029+6510*

The host galaxy of this object shows compact vigorous star formation within 2 kpc from the QSO. The rest of the galaxy seems to show no narrow Hα which we attribute to low star formation rates. SDSS 1029+6510 is the second most powerful QSO in our sample with a bolometric luminosity of 1.93×10^{47}erg s^{-1}(Table-1), in addition to the second longest observation time in our sample. The host galaxy kinematics reveals that the gas traced through narrow Hα is blue shifted with respect to the broad-line Hα from the QSO. Figure 5 shows the distribution of narrow-line Hα kinematics with a decrease in velocity at larger separations from the QSO, which may be reminiscent of an outflow extending over several kpc. A similar radial velocity map is present in a host galaxy of a QSO in Alexander et al. 2010 traced through broad [OIII] $\lambda5007$Å emission moving at comparable velocities (max velocity $\sim$ 300 km s^{-1}) but with a much broader velocity dispersion (364-935 km s^{-1}). The ratio

of $\log([NII]/H\alpha) < -1.5$ is located in the HII star formation portion of the BPT diagram for region B making it a strong candidate for star formation with a formation rate of of $67.4\pm5.7 M_\odot$ yr^{-1}. This indicates rapid star formation within 2kpc from the QSO.

For region C, a ratio of 0.57 ± 0.3 for $\log([NII]/H\alpha)$ puts this source partly in the ionization AGN region on the BPT diagram (Figure 6) and the detection of [NII] emission with higher signal to noise than Hα suggests this emission is due to the AGN. Lastly for region A, the measured ratio of $\log([NII]/H\alpha)=-0.6$ places it partially inside the star-formation region on the BPT diagram and the kinematics are likely due to dynamical interactions.

This source has a lack of extended star-forming regions, 90% of the star formation activity is within 2 kpc from the QSO. Resolved host galaxies in Inskip et al. 2011, Cano-Díaz et al. 2012 & Alexander et al. 2010 are far more extended, with star forming regions extending over several kpc(4-6kpc) with comparable star formation rates ($\sim$100 M$_\odot$ yr^{-1}). Our limiting flux simulations indicate that we should detect star formation rates as low as 1.4 M$_\odot$ yr^{-1} or down to a flux level of 0.6-0.8×10^{-17}erg s^{-1} cm^{-2}, at separations $>0.2''$ from the QSO. Instead, we detect two "streams" (region B at SNR>3) of narrow Hα and nothing else significant around it (regions A&C are $\sim 3\sigma$). This indicates that the surrounding (>2 kpc) regions have narrow Hα flux that is below the sensitivity of the instrument.

Simulations such as Hopkins & Elvis 2010 indicate that winds in the ISM can introduce turbulence into molecular clouds, effectively preventing new stars from forming in them. These winds tend to be driven through the interaction of winds/outflows from the vicinity of the black hole and the diffuse ISM. Due to the morphology of region B (extending from the QSO over several kpc) as well as its dynamical properties we speculate that this could be the AGN/star formation driven wind, that is illuminated by recent star formation within 2 kpc from the QSO.

Dust can cause an extinction of Hα flux by re-radiating it at longer wavelength. QSOs in their early stages of evolution are thought to be heavily obscured, after the AGN inputs energy/momentum during the "blow out" phase gas & dust can get pushed out allowing the AGN & galaxy to be detected in the optical, which otherwise would be obscured. Observations at other wavelengths can provide clues about the level of obscuration, a strong detection in the far-IR can indicate dust heating due to UV radiation from recent birth of massive stars. This would indicate that some portion of the UV radiation is absorbed (suppressed) and re-emitted at longer wavelength. QSOs that show reddening in their rest-frame UV spectra are good candidates for systems with a considerable level of obscuration, including a number of systems with indicators of outflows through blue shifted broad absorption lines in their rest-frame UV spectra, indicating that some of these systems might be in the "blow-out" stage (Farrah et al. 2012).

For the case of SDSS 1029+6510 we are able to put some constraints on the level of obscuration from both far-IR photometry and rest-frame UV-spectrum. This QSO was observed as part of a program with the Herschel space telescope to target some of the brightest optical QSOs with the SPIRE instrument. Examining the archival data we find that at the optical position of the QSO nothing is detected above 3σ level in the 250 μm, 350μm, and 500μm bands. The flux density limits are ($\sim$1mJy),indicating that this QSO's host galaxy is not in a star-burst phase (L$_{ir} < 10^{13}L_\odot$). The rest frame UV spectrum obtained from SDSS shows (Figure 1) a continuum slope typical of a type 1 un-obscured QSO (steep blue continuum), and a bolometric luminosity of 1.93×10^{47}erg s^{-1}, (Table-3) which is about an order of magnitude above the average QSO bolometric luminosity. Any correction for dust will start pushing the bolometric luminosity beyond the typical value for bright QSOs at z$\sim$ 2 ($\sim 10^{48}$erg s^{-1}). Assuming we need to correct an order of magnitude of flux at rest frame wavelength of 1450Å due to dust we would only push the limiting star formation rate to 0.7 M$_\odot$ yr^{-1} kpc^{-2} (using a Small Magellanic cloud extinction curve), not sufficient to explain the lack of Hα flux. We therefore favor the low star formation rate model as the main explanation for the observed Hα flux in the case of SDSS1029+6510 at separations greater than 2 kpc.

6.2. *SDSS 0925+06*

The extended Hα emission surrounding SDSS 0925+06 is a strong candidate for active star formation. The ratio of $\log([NII]/H\alpha)$ for region A is within the star formation region on the BPT diagram (Figure 6) while our limits on region B,C place them near the degenerate regions between star formation and AGN. The total flux from all these implies an integrated star formation rate of 29 M$_\odot$ yr^{-1}. Similar to SDSS 1029+6510 the detected narrow Hα emission is compact and we only detect narrow Hα in these three regions. In other regions of the data cube we are able to reach a sensitivity limit of 0.8×10^{-17}erg s^{-1}or a star formation rate of 1.4 M$_\odot$ yr^{-1} at separations $\gtrsim 0.2''$ from the QSO. All of the detected regions are at separations $\gtrsim 0.5''$ (4 kpc). This implies the narrow Hα flux sits below the sensitivity of the detector at separations between 1.4 to 4 kpc. As introduced in the §6.1 we propose that either halting of star formation or obscuration due to dust in the host galaxy to be the primary reasons for lack of Hα flux. The bolometric luminosity of this QSO as calculated from the 1450Å continuum is about an order of magnitude below the average value of a QSO at this redshift, due to the continuum being heavily reddened. However the broad Hα emission of this source agrees with the rest of the objects in our sample that do not show any signs of reddening in their rest-frame UV spectra (see Figure 1). All QSOs in our sample have typical bolometric luminosities of $\sim 3 \times 10^{46}$erg s^{-1}. The agreement between broad line Hα properties (velocity dispersion & intensity) hints that the bolometric luminosity should be consistent with the other members of our sample. As found in Fynbo et al. 2013 most reddened QSOs are red due to dust in their host galaxies rather than the inter-galactic medium or dust inside the Milky Way. For this source we estimate the amount of reddening by invoking the condition that the bolometric luminosity should be at the average value for a QSO with such a strong broad Hα emission (at least $\sim 3 \times 10^{46}$erg s^{-1}). This implies that the flux at 1450Å needs to be boosted

by $10^{0.94}$ implying that $A_{1450} = 2.35$. Using extinction curve from Gordon et al. 2003 assuming Small Magellanic Cloud(SMC) like extinction (R_v=2.74) we obtain $A_{H_\alpha} = 0.38$. This implies that the flux at Hα needs to be corrected by at least $10^{0.15}$, yielding a de-reddened star formation rate limit of 0.45 M$_\odot$ yr^{-1} kpc^{-2} , and the combined de-reddened star formation rate on A,B, and C of 41 M$_\odot$ yr^{-1} . This implies that dust attenuation only removes 0.1 M$_\odot$ yr^{-1} kpc^{-2} if we only correct the bolometric luminosity such that it sits at the average. Overall this level of dust obscuration is not enough to be the primary reason for low Hα flux.

Even assuming an extreme case where the bolometric luminosity is near the maximum value for a type-1 QSO at z~2 ($\sim 10^{48}$) would only imply a limit of 0.9M$_\odot$ yr^{-1} kpc^{-2}. This could imply that there is a low star formation rate in the host galaxy, where the star formation has been nearly shut off within $0.2''-0.5''$(1.4-4 kpc) from the QSO. These distant regions (A,B & C) are still forming stars at rates that are detectable. Our observations indicate that the host could be in a process of transitioning from a star-forming into a quiescent galaxy. However the less unlikely possibility is that the star formation is active in a diffuse region at separations of 1.4-4kpc rather than in the clumpy regions that we see in regions A,B,C and in other star forming galaxies at this redshift.

6.3. Comparison to other type-1 QSOs at z≳1

There has been a number of multi-wavelength surveys of radio quiet type 1 QSOs at z~2 that have presented a range of conclusions of host galaxy star formation properties. High redshift QSO studies have either implied high star formation rates in concurrent high-z type-I QSOs or have argued for a lack of star formation activity. In this section we summarize and compare surveys that share similar QSO properties to our sample (i.e., SMBH mass, bolometric luminosity, unobscured type 1).

Herschel PACS observations of AGNs & QSOs in the COSMOS extragalactic survey indicate a correlation between their bolometric luminosity and rest-frame 60μm host galaxy emission (Rosario et al. 2013). Using this relation, the bolometric luminosities of the QSOs in our sample indicates that the mean star formation rate should be of order 120 M$_\odot$ yr^{-1}. This is nearly an order of magnitude greater than the mean star formation rate in our sample, as indicated by narrow Hα emission line detection and limits. The disagreement between our sample and the Herschel results could be due to just the limited-number of sources observed (43 in Rosario et al. 2013 at a similar bolometric luminosity as the 6 QSOs in our sample). It is worth noting that the QSOs may be responsible for a significant portion of the total 60μm luminosity, so derived 60 μm star formation rates should be considered as upper limits.

HST observations of radio quiet QSOs at z~2 in Floyd et al. 2013 indicate an average star formation rate of 100 M$_\odot$ yr^{-1} derived from rest-frame UV emission originating from the host galaxy. In their study they use both stellar and artificial PSFs to remove the bright QSO. The number of QSOs in our sample is similar to Floyd et al. 2013, which share similar photometric properties. The star formation rate differences between our

sample and Floyd et al. 2013 could be due to strong QSO contamination from residual emission from their PSF subtraction, or that star formation in our hosts are quite diffuse.

In contrast, studies such as Villforth et al. 2008 and Kotilainen et al. 2009 find quiescent galaxies that host radio quiet high-z QSOs. These observations are from seeing-limited (0.4-0.5$''$) near-infrared imaging and are limited to disentangling the host galaxy at close angular scales ($\lesssim$ 4 kpc). SDSS0925+06 and SDSS0850+58 share similar observed magnitudes to these studies, yet the other half are 1 to 1.5 magnitudes brighter. Including our results, with these two other papers only yields a total of 15 high-z QSO that are observed to reside in "quiescent" z~2 galaxies.

At even higher redshifts, recent ALMA observations of z~6 QSOs (Wang et al. 2013; Willott et al. 2013) using the 158μm [CII] emission line reveals a detection in nearly 90% of the sources observed. The targets in their samples have similar properties to ours (i.e., BH mass, bolometric luminosities & Eddington ratios). In Willott et al. 2013 they reach a star formation limit of 40 M$_\odot$ yr^{-1} assuming the [CII] emission emanates solely from star formation. Yet sources in Wang et al. 2013 reach star formation rates as high as 1000 M$_\odot$ yr^{-1}, which implies that sources with detected [CII] have extreme star formation rates in comparison to our detections and sensitivity limits at z=2. These z~6 sources are all near the peak of their starburst phase, assuming that most of the [CII] emission originates from star formation and not the QSO. According to present day M$_{stellar,bulge}$-M$_{bh}$ relation and theoretical work (e.g., Somerville et al. 2008) there is an expectation of simultaneous SMBH and galaxy growth (i.e., via mergers). In contrast, our observations show star formation rates that are well below this expected initial burst and below the typical star-forming galaxies at z~2 (Erb et al. 2006; Förster Schreiber et al. 2009; Steidel et al. 2014).

The essential difference (and advantage) of our study compared to previous studies, is that our detection and limits of star formation rates can be made at differing spatial and velocity locations away from the QSO. Whereas, the majority of all studies we have discussed have integrated star formation rate limits over a large range of PSF and beam sizes. Based on our detection limits, it is clear that we do not detect the clumpy (1 kpc^2), strong star formation regions (up to ~10 M$_\odot$ yr^{-1} kpc^{-2}) in current IFS observed z~2 star forming galaxies (Förster Schreiber et al. 2009; Law et al. 2009; Genzel et al. 2011; Law et al. 2012). If there is underlying star formation undetected in these host systems, then the surface brightness profiles of the star formation has to be diffuse and integrated across a large area of the galaxy. If our limits are to match previous inferred star formation rates of z~2 QSO hosts, then it would need to be diffuse with significant extinction.

The sample selection in our pilot survey is albeit random since we were selecting based on achieving the best AO performance for PSF subtraction, therefore it is interesting that we would happen to select 5/6 type-I QSOs that are quiescent. The majority of our sample is similar to only a little number of observations of high-z QSO host residing in quiescent galaxies, and are in disagree-

ment to other work that indicate simultaneous high star formation rates. QSO duty cycles are still poorly understood, however it does seem to appear that in a number of cases the QSO can still be active while star formation in the host has been effectively turned off. These results agree well with AGN feedback models that require that the feedback mechanism only carry a small portion of the total bolometric luminosity of the QSO (5-10%) to effectively turn off star formation (Hopkins & Elvis 2010). However, our study and Kotilainen et al. 2009; Villforth et al. 2008 studies are also consistent with star formation time scales being significantly shorter than that of the QSO. There is likely numerous high angular resolution observations from HST and ground-based observations that have had null detections of high-redshift QSO host galaxies, that would benefit being released to the community to improve these global statistics. Interestingly, this means there is likely a social selection bias of high-z QSO host galaxies, where authors typically only publish detections (hence QSO hosts with higher star formation properties) rather than their null detections. In any case, it is obvious that there are a large number of selection effects that need to be taken account, but clearly a larger sample of high-redshift QSOs would greatly benefit from IFS+AO observations and aid in our understanding of the demographics of high-z QSO host galaxies.

7. CONCLUSIONS

We have presented LGS-AO assisted integral field spectroscopy observations of five $z = 2$ QSOs targeted at resolving Hα nebular emission lines from their host galaxies. Using the broad emission line region of the QSO we were able to construct a PSF to remove the QSO continuum and emission to achieve the necessary contrast to detect Hα and [NII] host galaxy emission.(see §4).

- For two out of five sources (SDSS 1029+6510 & SDSS 0925+06) we are able to resolve extended narrow line emission surrounding the QSO.

- In SDSS 1029+6510 we detect narrow Hα (region A and B) that likely originates from star formation at close separations (2 - 4 kpc) to the QSO. If we assume the Hα flux is from star formation the integrated star formation rate from region A and B is 78.4±6.2 M$_\odot$ yr^{-1}(110 M$_\odot$ yr^{-1} with dust correction).

- For SDSS 0925+06 we detect three distinct star forming regions that are separated from the QSO by $\sim$ 4 kpc. The upper limit star formation rate for all three regions combined is 29.0±2.4 M$_\odot$ yr^{-1}(40.7 M$_\odot$ yr^{-1} with dust corrections).

- Careful examination of the other three sources in our sample do not detect any narrow Hα emission post PSF subtraction, even in the cases of SDSS1005+4356 & SDSS2123-00 for which we spent the most integration time per source.

- We ran a Monte Carlo simulation on our data by inserting extended narrow Hα at various separations from the QSO with varying Hα fluxes (star formation rates). We find that we can detect star formation rates down to 1.4 M$_\odot$ yr^{-1} (see §5.3) as close as 0.2″ from the QSO. Incorporating dust obscuration this value can vary from 0.3M$_\odot$ yr^{-1} kpc^{-2} - 0.8M$_\odot$ yr^{-1} kpc^{-2} (see §6.1 & §6.2) depending on the value of A$_V$. At these limits, after correcting the SDSS spectra for dust reddening we are pushing the bolometric luminosities for some of our sources past the typical values for type 1 QSOs at this redshift. Even with a star formation rate of 0.8 M$_\odot$ yr^{-1} kpc^{-2} it would be difficult to explain the main cause of missing narrow Hα to be due to dust obscuration inside the host galaxy. Hence for these sources low star formation rates is the likely reason for lack of narrow Hα originating from the host galaxy.

- Three sources show low star formation rates at close angular separation of the QSO, with no dereddened star formation $\gtrsim$ 0.8 M$_\odot$ yr^{-1} kpc^{-2} within 2 to 4 kpc of the QSO.

- Compared to other z=2 QSO host galaxy surveys our sample is unique by having little-to-no star formation in high redshift type-I QSOs. This is in agreement with a large fraction of nearby (z $\lesssim$ 0.5) QSO host galaxies being quiescent. Yet at comparable and higher redshifts to our sample the majority of surveys have found simultaneous star formation activity with QSO activity. Clearly more work developing a larger z=1-3 QSO IFS+AO sample with a better defined sample selection will aid in developing a more coherent picture of QSO host galaxies in the early universe.

REFERENCES

Alexander, D. M., Swinbank, A. M., Smail, I., McDermid, R., & Nesvadba, N. P. H. 2010, MNRAS, 402, 2211

Alexander, D. M., & Hickox, R. C. 2012, New A Rev., 56, 93

Allen, M. G., Groves, B. A., Dopita, M. A., Sutherland, R. S., & Kewley, L. J. 2008, ApJS, 178, 20

Bahcall, J. N., Kirhakos, S., Saxe, D. H., & Schneider, D. P. 1997, ApJ, 479, 642

Barai, P., Viel, M., Murante, G., Gaspari, M., & Borgani, S. 2014, MNRAS, 437, 1456

Becker, R. H., White, R. L., & Helfand, D. J. 1995, ApJ, 450, 559

Bennert, N., Canalizo, G., Jungwiert, B., et al. 2008, ApJ, 677, 846

Cano-Díaz, M., Maiolino, R., Marconi, A., et al. 2012, A&A, 537, L8

Cardelli, J. A., Clayton, G. C., & Mathis, J. S. 1989, ApJ, 345, 245

Carniani, S., Marconi, A., Biggs, A., et al. 2013, A&A, 559, A29

Croom, S. M., Richards, G. T., Shanks, T., et al. 2009, MNRAS, 399, 1755

Cutri, R. M., Skrutskie, M. F., van Dyk, S., et al. 2003, "The IRSA 2MASS All-Sky Point Source Catalog, NASA/IPAC Infrared Science Archive

Davies, R. I. 2007, MNRAS, 375, 1099

Di Matteo, T., Springel, V., & Hernquist, L. 2005, Nature, 433, 604

Erb, D. K., Steidel, C. C., Shapley, A. E., et al. 2006, ApJ, 647, 128

Fabian, A. C. 2012, ARA&A, 50, 455

Falomo, R., Kotilainen, J. K., Pagani, C., Scarpa, R., & Treves, A. 2004, ApJ, 604, 495

Falomo, R., Kotilainen, J. K., Scarpa, ., & Treves, A. 2005, A&A, 434, 469

Farrah, D., Urrutia, T., Lacy, M., et al. 2012, ApJ, 745, 178

Floyd, D. J. E., Axon, D., Baum, S., et al. 2010, ApJ, 713, 66

Floyd, D. J. E., Dunlop, J. S., Kukula, M. J., et al. 2013, MNRAS, 429, 2

Förster Schreiber, N. M., Genzel, R., Bouché, N., et al. 2009, ApJ, 706, 1364

Fynbo, J. P. U., Krogager, J.-K., Venemans, B., et al. 2013, ApJS, 204, 6

Gebhardt, K., Bender, R., Bower, G., et al. 2000, ApJ, 539, L13

Genzel, R., Newman, S., Jones, T., et al. 2011, ApJ, 733, 101

Gordon, K. D., Clayton, G. C., Misselt, K. A., Landolt, A. U., & Wolff, M. J. 2003, ApJ, 594, 279

Harrison, C. M., Alexander, D. M., Mullaney, J. R., & Swinbank, A. M. 2014, arXiv:1403.3086

Hopkins, P. F., & Quataert, E. 2011, MNRAS, 415, 1027

Hopkins, P. F., & Elvis, M. 2010, MNRAS, 401, 7

Liu, G., Zakamska, N. L., Greene, J. E., Nesvadba, N. P. H., & Liu, X. 2013, MNRAS, 436, 2576

Hamilton, T. S., Casertano, S., & Turnshek, D. A. 2002, ApJ, 576, 61

Hutchings, J. B., Frenette, D., Hanisch, R., et al. 2002, AJ, 123, 2936

Inskip, K. J., Jahnke, K., Rix, H.-W., & van de Ven, G. 2011, ApJ, 739, 90

Kornei, K. A.,Shapley, A. E., Martin, C. L., et al. 2012, ApJ, 758, 135

Kotilainen, J. K., Falomo, R., Decarli, R., et al. 2009, ApJ, 703, 1663

Kauffmann, G., Heckman, T. M., Tremonti, C., et al. 2003, MNRAS, 346, 1055

Kennicutt, R. C., Jr. 1998, ApJ, 498, 541

Kewley, L. J., Dopita, M. A., Sutherland, R. S., Heisler, C. A., & Trevena, J. 2001, ApJ, 556, 121

Kirhakos, S., Bahcall, J. N., Schneider, D. P., & Kristian, J. 1999, ApJ, 520, 67

Larkin, J., Barczys, M., Krabbe, A., et al. 2006, New A Rev., 50, 362

Law, D. R., Steidel, C. C., Erb, D. K., et al. 2009, ApJ, 697, 2057

Law, D. R., Shapley, A. E., Steidel, C. C., et al. 2012, Nature, 487, 338

Lehnert, M. D., van Breugel, W. J. M., Heckman, T. M., & Miley, G. K. 1999, ApJS, 124, 11

Magorrian, J., Tremaine, S., Richstone, D., et al. 1998, AJ, 115, 2285

Márquez, I., & Petitjean, P. 2003, Revista Mexicana de Astronomia y Astrofisica Conference Series, 16, 135

Matsuoka, Y., Strauss, M. A., Price, T. N., III, & DiDonato, M. S. 2014, ApJ, 780, 162

McConnell, N. J., & Ma, C.-P. 2013, ApJ, 764, 184

McGregor, P. J., Hart, J., Conroy, P. G., et al. 2003, Proc. SPIE, 4841, 1581

O'Donnell, J. E. 1994, ApJ, 422, 158

Pettini, M., & Pagel, B. E. J. 2004, MNRAS, 348, L59

Planck Collaboration, Ade, P. A. R., Aghanim, N., et al. 2013, arXiv:1303.5076

Quinlan, G. D., & Hernquist, L. 1997, New A, 2, 533

Somerville, R. S., Hopkins, P. F., Cox, T. J., Robertson, B. E., & Hernquist, L. 2008, MNRAS, 391, 481

Ridgway, S., Heckman, T., Calzetti, D., & Lehnert, M. 2002, New A Rev., 46, 175

Riechers, D. A., Walter, F., Carilli, C. L., Bertoldi, F., & Momjian, E. 2008, ApJ, 686, L9

Rosario, D. J., Trakhtenbrot, B., Lutz, D., et al. 2013, A&A, 560, A72

Runnoe, J. C., Brotherton, M. S., & Shang, Z. 2012, MNRAS, 422, 478

Sesana, A., Haardt, F., & Madau, P. 2008, ApJ, 686, 432

Scannapieco, E., Silk, J., & Bouwens, R. 2005, ApJ, 635, L13

Schaerer, D., Boone, F., Zamojski, M., et al. 2014, arXiv:1407.5793

Schneider, D. P., Richards, G. T., Hall, P. B., et al. 2010, AJ, 139, 2360

Schramm, M., Wisotzki, L., & Jahnke, K. 2008, A&A, 478, 311

Shen, Y., & Liu, X. 2012, ApJ, 753, 125

Steidel, C. C., Rudie, G. C., Strom, A. L., et al. 2014, arXiv:1405.5473

2005ApJ...630..167T Thompson, T. A., Quataert, E., & Murray, N. 2005, ApJ, 630, 167

Veilleux, S., Kim, D.-C., Rupke, D. S. N., et al. 2009, ApJ, 701, 587

Villforth, C., Heidt, J., & Nilsson, K. 2008, A&A, 488, 133

Wang, R., Wagg, J., Carilli, C. L., et al. 2013, ApJ, 773, 44

Wang, J.-G., Dong, X.-B., Wang, T.-G., et al. 2009, ApJ, 707, 1334

Willott, C. J., Omont, A., & Bergeron, J. 2013, ApJ, 770, 13

Wurster, J., & Thacker, R. J. 2013, MNRAS, 431, 2513

Zakamska, N. L., Strauss, M. A., Krolik, J. H., et al. 2006, AJ, 132, 1496

Vayner et al. 2014

TABLE 1
OBSERVATIONAL SUMMARY

QSO	R.A J2000	DEC J2000	$z_{H\alpha}$	Observation Date	Integration $N_{frames}\times$s	PSF FWHM $''$	Tip/Tilt sep ($''$)
SDSS0850+58	08:50:22.63	+58:43:15	2.211	2013Jan04	4x600	0.15	14.1
SDSS0925+06	09:25:47.47	+6:55:38.9	2.196	2013Jan08	6x600	0.13	6.2
SDSS1005+43	10:05:17.50	+43:46:10.9	2.105	2011Dec31	16x300	0.202	47.8
SDSS1029+65	10:29:07.09	+65:10:24.61	2.182	2011Dec30	12x300	0.177	47.6
SDSS2123−00	21:23:29.46	−00:50:52.9	2.281	2012Aug06	6x600	0.11	0

TABLE 2
SDSS & 2MASS PHOTOMETRY (CUTRI ET AL. 2003)

QSO	u	g	r	i	z	J	H	K
SDSS0850+58	19.301	19.071	18.939	18.977	18.619	−	−	−
SDSS0925+06	21.583	20.745	19.888	19.493	19.197	−	−	−
SDSSJ1005+4346	16.985	16.803	16.631	16.469	16.249	15.474	15.041	14.271
SDSSJ1029+6510	17.150	16.938	16.833	16.757	16.602	15.881	15.413	14.566
SDSS2123−00	17.194	16.648	16.434	16.338	16.121	15.180	14.616	13.904

TABLE 3
QSO GENERAL PROPERTIES

QSO	z_{UV}	L_{Bol} erg s^{-1}	M_{BH} log(M$_\odot$)	Eddington Ratio
SDSS0850+58	2.211	3×10^{46}	9.15	0.18
SDSS0925+06	2.197	$\cdots$	9.21	$\cdots$
SDSS1005+43	2.086	1.88×10^{47}	9.59	0.4
SDSS1029+65	2.163	1.93×10^{47}	9.58	0.4
SDSS2123−00	2.261	2.5×10^{47}	9.74	0.4

Column 3 is the bolometric luminosities obtained from rest frame 1450Å continuum with corrections from Runnoe et al. 2012. Column 4 is the black hole mass obtained either from rest frame 1549Å CIV (Shen & Liu 2012) or from 2800ÅMgII (Wang et al. 2009) emission lines, when the rest frame 3000Å continuum is in the SDSS spectral band. Column 5 is the ratio of the bolometric luminosity to the Eddington luminosity obtained from the measured black hole mass.

TABLE 4
BROAD LINE EMISSION REDSHIFTS

QSO	Lyα		CIV		CIII		MgII		Hα	
	z	v_{offset}	z	v_{offset}	z	v_{offset}	z	v_{offset}	z	v_{offset}
SDSS0850+58	2.20841±0.00074	94.63	2.1990±0.0015	-779.30	2.1821±0.0019	-704.75	2.210±0.014	316.61	2.21156±0.00028	388.42
SDSS0925+06	2.19879±0.00038	435.16	2.1963±0.0092	205.28	2.1999±0.0055	-1127.42	2.196±0.015	190.52	2.19554±0.00014	129.74
SDSS1005+43	⋯	⋯	2.08684±0.00047	-268.36	2.0907±0.0020	111.223	2.1010±0.0060	1106.52	2.10484±0.00023	1480.25
SDSS1029+65	2.1778±0.0082	1566.45	2.15352 ±0.00063	-737.78	2.1622±0.0017	92.998	2.1778±0.0019	1566.72	2.18295±0.00011	1906.98
SDSS2123−00	2.2785±0.0082	1411.92	2.25292±0.00082	-945.60	2.2621±0.0029	-100.73	2.2705±0.0029	675.52	2.28074±0.00012	1611.98

TABLE 5
PROPERTIES OF BROAD-LINE Hα EMISSION

QSO	$z_{H\alpha}$	$L_{H\alpha}$ erg s^{-1}	M_{BH} log(M$_\odot$)	Equivalent Width (Å)
SDSS0850+58	2.211	3.26×10^{44}	9.24	75.59±0.96
SDSS0925+06	2.196	2.52×10^{44}	9.21	44.96±0.14
SDSS1005+43	2.105	7.42×10^{44}	10.96	71.42±0.32
SDSS1029+65	2.182	3.26×10^{44}	9.37	76.32±0.47
SDSS2123−00	2.281	3.95×10^{44}	9.6	66.07±0.17

Column 3 is the luminosity of the broad Hαline. Column 4 is the black hole mass derived from Hα FWHM and its luminosity as in Shen & Liu 2012. Column 5 is the equivalent width of the broad Hαline.

TABLE 6
SDSSJ1029+65: OSIRIS-AO NARROW EMISSION-LINE PROPERTIES

Component	$F_{H\alpha}$	$F_{[NII]}$	[NII]/Hα	SFR M$_\odot$ yr^{-1}	V_r km s^{-1}	V_σ km s^{-1}	M_{dyn}
A	4.22 ± 0.75	<0.951	<0.2310	· · ·	-778±16	163±36	· · ·
B	22.6 ± 1.92	<0.71	<0.0319	67±6	-355±19	34±12	0.9
C	4.14± 1.95	2.34±0.73	0.570± 0.32	· · ·	-39±42	36±40	· · ·

Column 2 and 3 are in units of erg s^{-1} cm^{-2} × 10^{-17}. Column 8 is in units of M$_\odot$ × 10^9.

TABLE 7
SDSSJ0925+06: NIFS-AO NARROW EMISSION-LINE PROPERTIES

Component	$F_{H\alpha}$	$F_{[NII]}$	[NII]/Hα	SFR M$_\odot$ yr^{-1}	V_r km s^{-1}	V_σ km s^{-1}	M_{dyn}
A	4.33±1.22	<0.245	<0.0565	13±2.3	88.4±19.6	103.1±19.3	8.7
B	4.11±0.163	<0.58	<0.1410	12±0.5	242.6±15.4	37.7±14.5	1.0
C	1.20±0.126	<0.148	<0.1222	4±0.4	250.5±15.6	42.44±14.7	0.3

Column 2 and 3 are in units of erg s^{-1} cm^{-2} × 10^{-17}. Column 8 is in units of M$_\odot$ × 10^9.
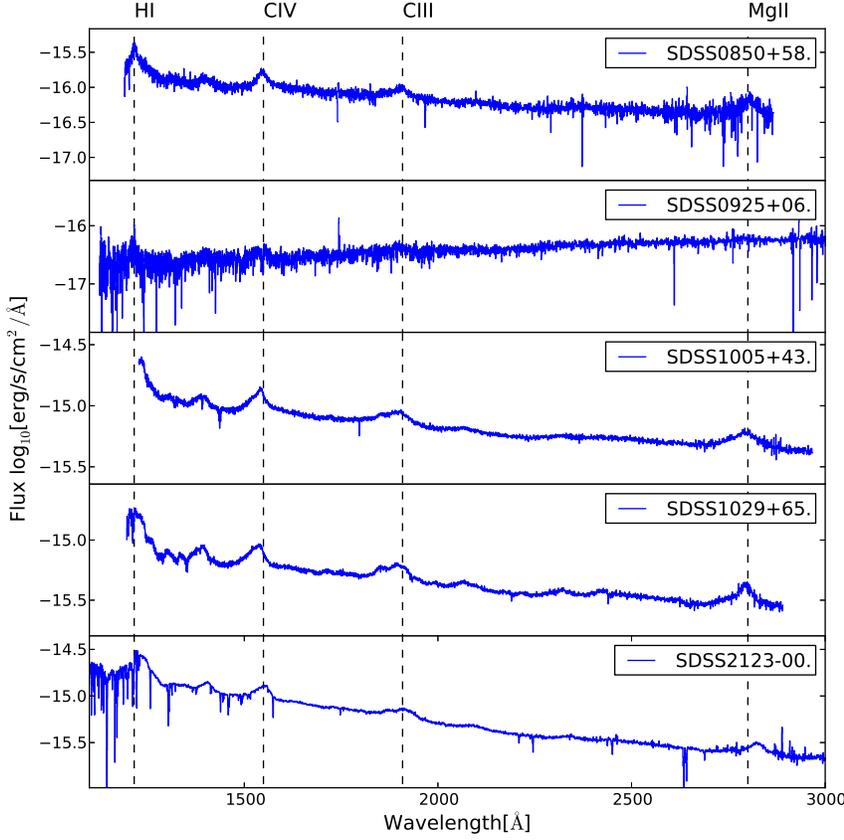
FIG. 1.— SDSS spectra of all the sources in our sample. The SDSS wavelength range covers the rest frame UV emission lines of QSOs at this redshift.The vertical dashed lines indicate the emission from Lyα, CIV, CIII, MgII.
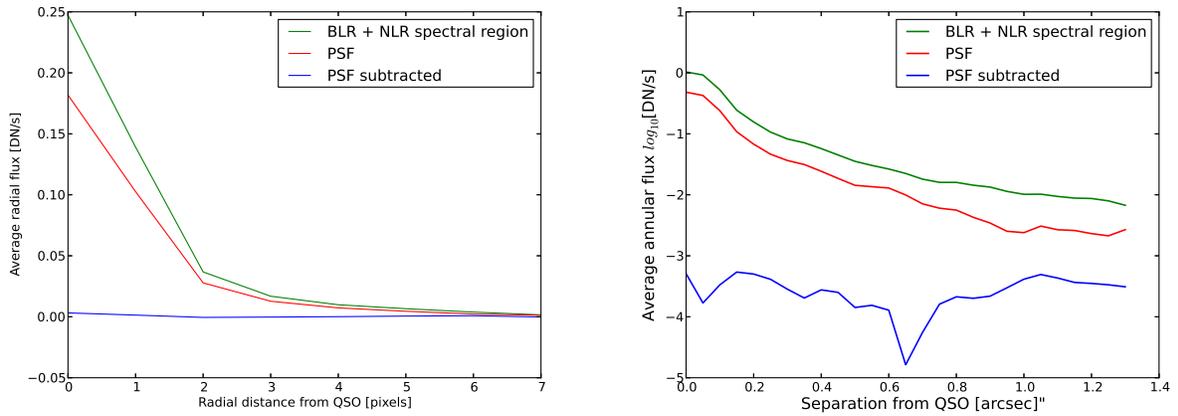

FIG. 2.— Radial profiles for SDSSJ1029+6510 (left) and SDSS0925+06(right), the green and blue radial profile curves are constructed from a spectrally collapsed images which contains both broad and narrow Hα while the red curve is constructed from the PSF image. The blue curve is constructed in the same spectral regions as the green curve however post PSF subtraction, indicating that our PSF removal technique is capable of removing both the AO corrected core as well as the seeing halo. halo.
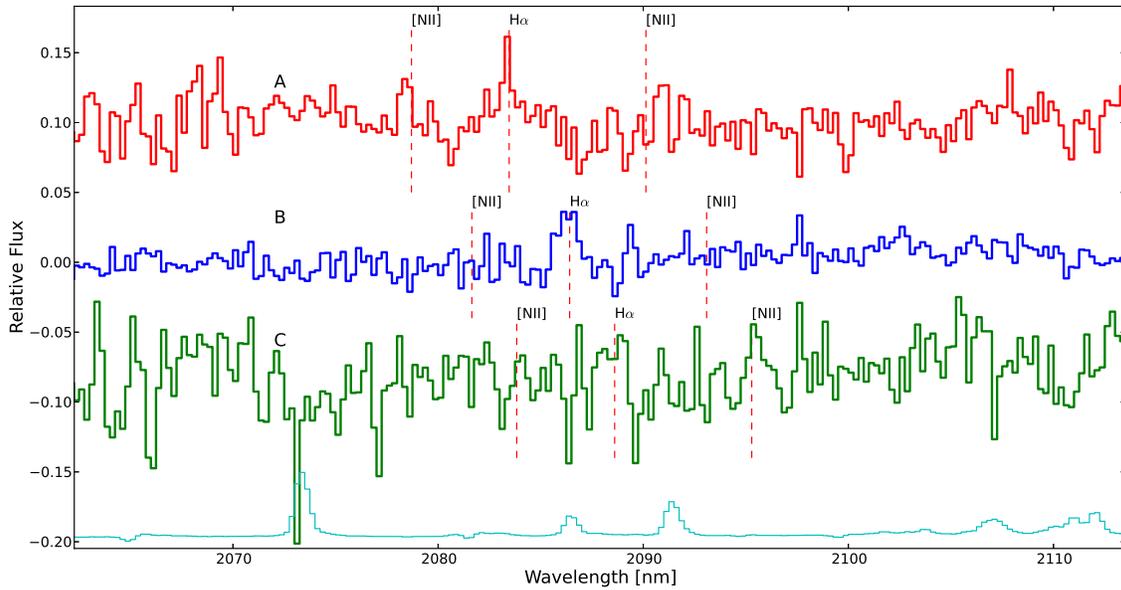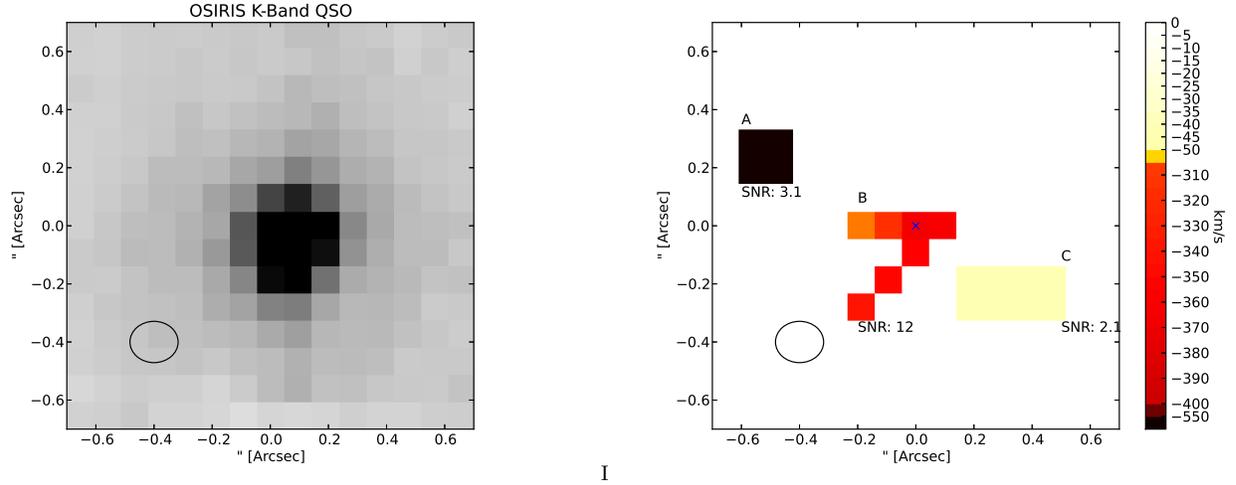
Fig. 3.— Upper left: K-Band image of SDSSJ1029+6510 from the collapsed OSIRIS LGS-AO data cube using the 0.1″ spatial sampling. Upper right: radial velocity map (km s^{-1}) of the extended narrow Hα emission detected post PSF subtraction. Radial velocity measurements are obtained by fitting the narrow Hα emission line in the individual regions with a Gaussian function. Bottom: Spectra of each of the labeled components with some relative flux offset. The spatial resolution of each observation is repressed by the ellipse in the lower left corner obtained through 2D Gaussian fitting to the PSF image. The light blue curve shows the wavelength dependence of the noise and OH sky. emission.
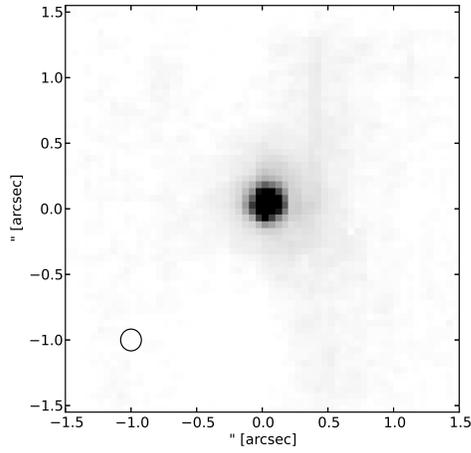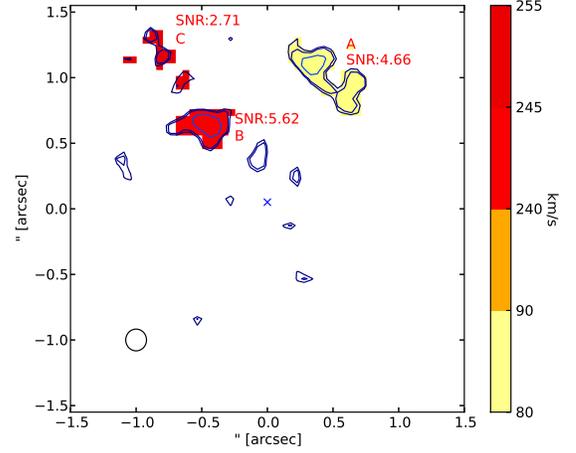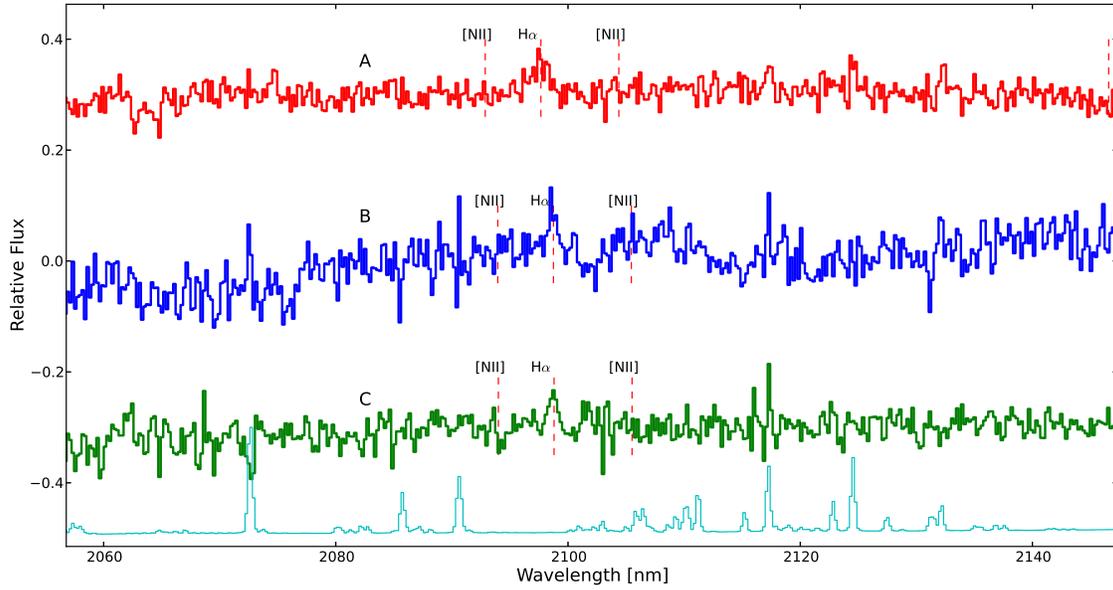
FIG. 4.— Upper left: K-Band image of SDSS0925+06 from the collapsed NIFS Altair AO cube using the 0.5″ spatial sampling. Upper right: PSF subtracted image showing resolved extended Hα narrow line emission (contours) & and the velocity map (km s⁻¹) obtained from fitting the Hα line in the individual regions using a Gaussian function. Bottom: Spectra of each of the labeled components with some relative flux offset. The spatial resolution of each observation is repressed by the aperture in the lower left corner obtained through 2D Gaussian fitting to the PSF image. The light blue curve shows the wavelength dependence of the noise and OH sky.
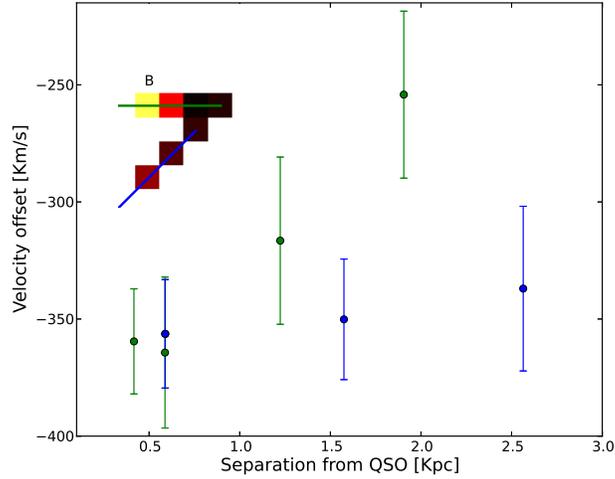
FIG. 5.— Velocity offset (km s^{-1}) relative to the redshift of the broad Hα emission in region B, as a function of projected separation (kpc) from the centroid of the SDSS 1029+6510 QSO. Inserted in the top-left corner is the velocity map of region B, as seen in Figure 3. On top of the velocity map the color coded slits are presented to illustrate the two trends in the radial velocity curves (green and blue). The radial velocity profile shows that for both "wings" the kinematics do not agree with a rotating disc, but rather a weak outflow.
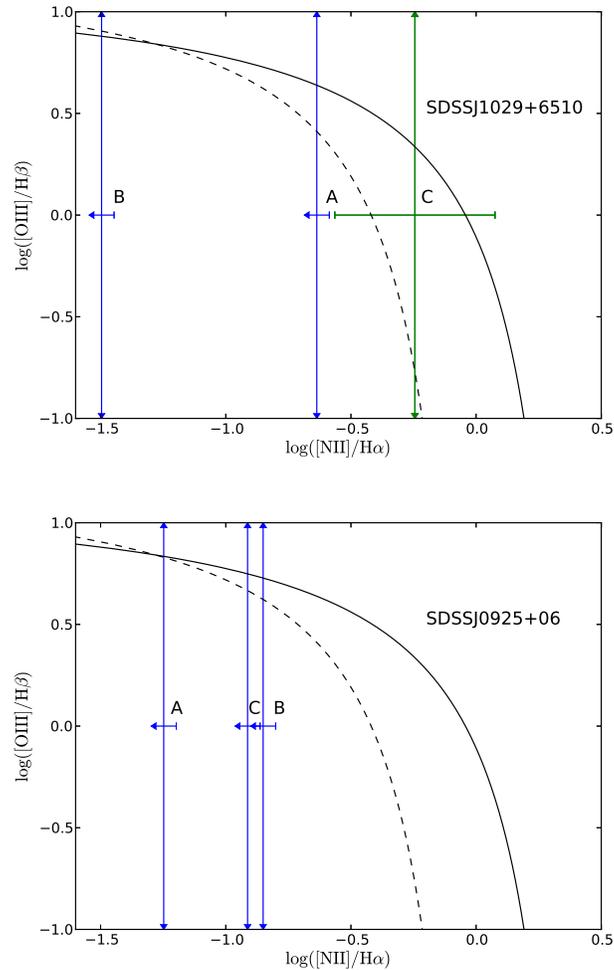

FIG. 6.— Line ratio diagnostics for our detected narrow-line emission using the standard BPT diagram, log([OIII]/Hβ) and log([NII]/Hα) for SDSSJ1029+6510 regions A,B & C (TOP) and regions A,B, & C over plotted for SDSSJ0925+06 (BOTTOM). The blue points are likely Overlaid is the empirical limit between star formation and AGN from the SDSS survey (z<0.1) by Kauffmann et al. 2003. The solid curve is the theoretical star formation limit from Kewley et al. 2001. The blue points are locations in the diagram where they Hαemission is likely due to star formation, where are the green point for region C (top) is likely emanating from AGN ionization.
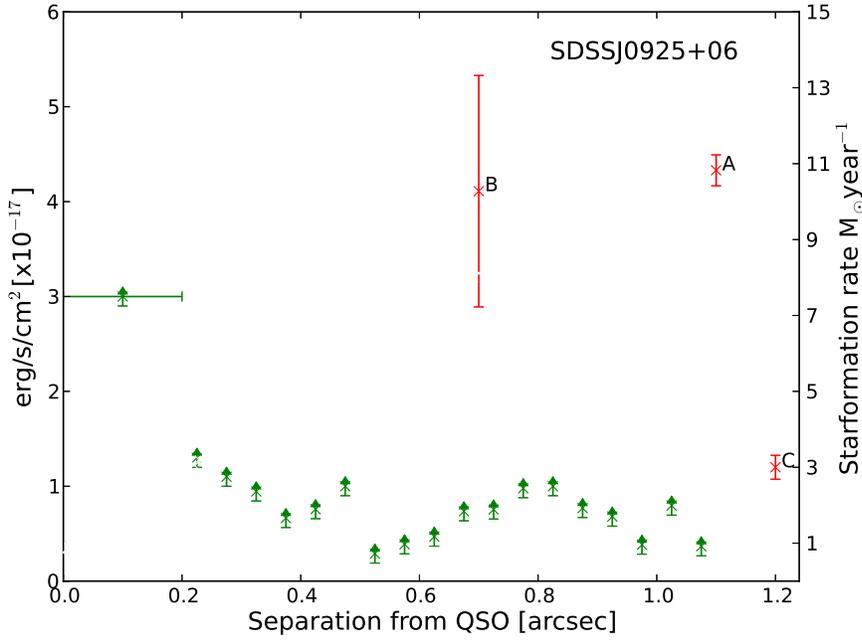
FIG. 7.— Limiting flux that was recovered at various distances from the QSO in our Monte Carlo simulations from the NIFS observations of SDSS 0925+06 (green). Fluxes of features A,B,C (red) from Figure 4 are over plotted.
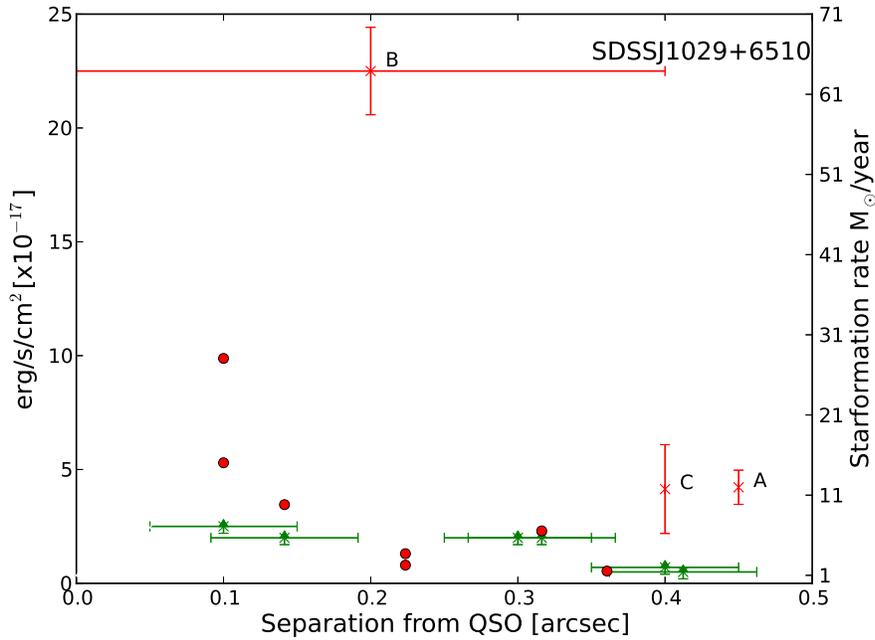

FIG. 8.— Limiting flux that was recovered at various distances from the QSO in our Monte Carlo simulation from the OSIRIS observations of SDSS 1029+6510 (green). Fluxes and distribution of features A,B,C (light red) from Figure 3 are over plotted. In addition, flux from individual spaxels from region B are plotted in dark red. Some individual spaxels do not surpass the flux limit, but when integrated produce a spectrum with a significant signal-to-noise that is above the noise floor.